CHAPTER 2

STRUCTURES AND PHOTOLUMINESCENCE PROPERTIES OF LANTHANIDE-PYRIDINE-2,6-DICARBOXYLATES

2.1 Introduction

Over the last decade, pyridine-2,6-dicarboxylic acid (H_2pdc) have been regularly chosen as organic ligand for the construction of Ln-CPs. This is due to the fact that H_2pdc exhibits strong coordination stability, rich coordination modes, plentiful π-π and hydrogen bonding interactions which are necessary in stabilizing coordination structures [1,2]. It is worth noted that hydrogen bonding interactions not only help in the self-assembly processes, but they can also facilitate supramolecular assembly of the hydrogen-bonded MOFs [2]. In solid state structures, H_2pdc may be presented in the non-deprotonated (H_2pdc), the partially deprotonated ($Hpdc^-$) or the fully deprotonated (pdc^{2-}) forms. Referring to the Cambridge Structure Database [3], there are only few examples of CPs made up of Ln^{III} ions and $Hpdc^-$ or H_2pdc compared with those based on the fully deprotonated pdc^{2-}. It may be due to the fact that the presence of the protonated carboxylate groups in the Ln complexes tends to give structures with low stability, because of their prohibition in the formation of multi-dimensional coordination network with higher stability [4-7].

Controllable preparation of the crystalline Ln-CPs is still a challenge since many factors in the synthesis, such as solvent, counter ion, pH as well as the synthetic method, exhibits important influences on the nucleation and crystallization process [8-10]. Different synthetic methods can lead to diverse products (including different molecular formula, structure, and dimensionality) even when the same reactants (metal, ligand, and solvent) are employed [11]. The synthetic method may also insert drastic effect on reaction time, yield and crystal size [12]. Nevertheless, there are very few literatures reported on the influences of these factors on structural variation of Ln-CPs.

In this chapter, the synthesis and structural characterization of ten Ln-CPs using H_2pdc of different degree of deprotonation as organic linkers is reported. The as-synthesized structures are classified to three different groups according to their structural symmetries; (i) the cubic $Pa\bar{3}$ structures of $[Ln(pdc)(H_2O)_4]_3 \cdot 3Cl$ where Ln = Pr (**I**), Nd (**II**), Sm (**III**), Eu (**IV**), and Gd (**V**), (ii) the monoclinic $P2_1/c$ structures of $[Ln(pdc)(Hpdc)(H_2O)_2] \cdot 3H_2O$ where Ln = Pr (**VI**), Nd (**VII**), and Sm (**VIII**), and (iii) the cubic $Ia\bar{3}$ structures of $[Ln(pdc)(H_2O)_4]_3 \cdot 3Cl$ where Ln = Sm (**IX**), and Eu (**X**). The influences of two heating techniques with different heating mechanism and kinetics, namely the conventional heating under reflux and the dielectric microwave heating, on the final structures have been investigated. The template effect of the chloride anion in the formation of the 3D $[Ln(pdc)(H_2O)_4]_3 \cdot 3Cl$, for example, was examined compared with the formation of the 1D $[Ln(pdc)(Hpdc)(H_2O)_2] \cdot 3H_2O$. Hirshfeld surface analyses of the 1D $[Ln(pdc)(Hpdc)(H_2O)_2] \cdot 3H_2O$ is also included. Thermogravimetric and photoluminescence properties of selected complexes are discussed.

2.2 Experimental

2.2.1 Materials and methods

$PrCl_3 \cdot 6H_2O$, $NdCl_3 \cdot 6H_2O$, $SmCl_3 \cdot 6H_2O$, $EuCl_3 \cdot 6H_2O$ and $GdCl_3 \cdot 6H_2O$ were first prepared by dissolving Pr_6O_{11} (TJTM, 99.9%), (Nd_2O_3 (TJTM, 99.99%), Sm_2O_3 (TJTM, 99.5%), Eu_2O_3 (Merck, 99%) and Gd_2O_3 (Sigma-Aldrich, 99.9%), accordingly, in the excess amount of HCl(aq) (BDH, 37%). The solutions were heated to evaporate the HCl(aq) and reach supersaturation from which the crystals of $LnCl_3 \cdot 6H_2O$ crystallized. Amounts of the crystallizing water were evaluated by thermogravimetric analyses. Pyridine-2,6-dicarboxylic acid (H_2pdc; $C_7H_5NO_4$, Fluka, >98%) and ethanol (C_2H_5OH; Merck, 95%) were obtained commercially and used without further purification.

Powder X-ray diffraction (PXRD) experiments were conducted using a Rigaku Mini Flex II X-ray diffractometer operated with Cu K_α radiation (λ = 1.5418 Å, 40 kV, 15 mA). Infrared (IR) spectra were recorded on a Bruker Tensor 27 FT-IR instrument using potassium bromide (KBr; BDH, 98.5%) discs. The UV-Vis spectra were collected on the suspension of 0.2500 mM of ground crystals in 10.00 mL DI water, using UV-Vis spectrophotometer (Perkin Elmer, Lambda25, USA). Photoluminescence (PL) spectra

were performed at room temperature using an Avantes Multichannel spectrometer with the Ocean Optics LED 255 nm excitation source.

2.2.2 Crystal growth and characterization

Two synthetic methods, namely the microwave heating and the conventional heating under reflux, were employed in the preparation and crystal growth of ten complexes as summarized in Fig. 2.1.

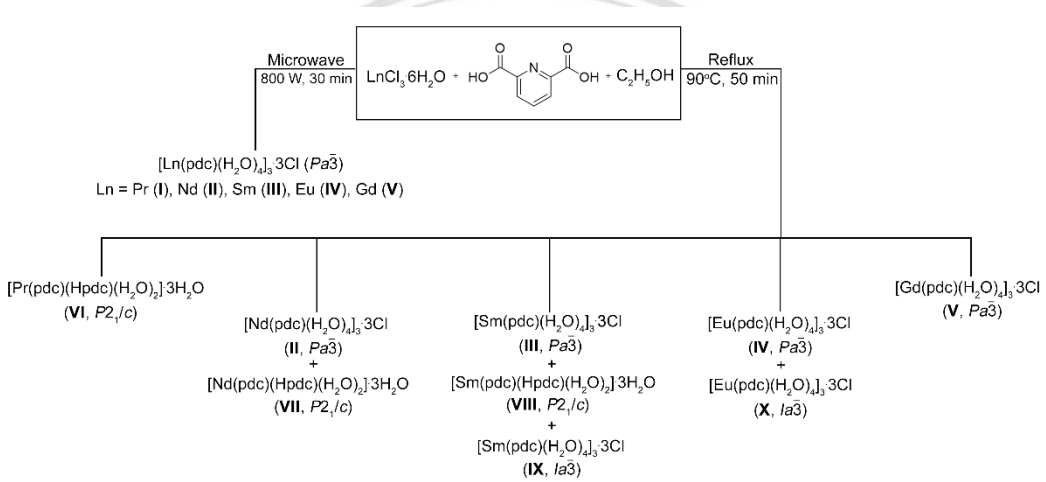

Fig. 2.1 Diagrammatic scheme summarizing the syntheses and the yielded products.

Microwave synthesis. $LnCl_3 \cdot 6H_2O$ (0.0355-0.0372 g, 0.100 mmol) and H_2pdc (0.0167 g, 0.100 mmol) were dissolved in ethanol (10.00 mL) using a Teflon vessel. After the vessel was sealed and placed in the household microwave oven (Samsung MS23F301E), the reaction was conducted at 800 W for 30 min. After the reaction was cooled down to room temperature, the crystals of $[Ln(pdc)(H_2O)_4]_3 \cdot 3Cl$ {$Pa\bar{3}$; Ln = Pr (**I**), Nd (**II**), Sm (**III**), Eu (**IV**) and Gd (**V**)}, accordingly, were obtained in few days.

Heating under reflux. The reaction mixtures of the same molar ratios as those employed for the microwave assisted syntheses were heated at 90˚C under reflux for 50 min and left to cool down to room temperature. Crystals of similar habits to those obtained from the microwave syntheses were obtained in few days. The PXRD and the single crystal X-ray diffraction results indicated the yielding of five more distinct crystals; $[Ln(pdc)(Hpdc)(H_2O)_2] \cdot 3H_2O$ {$P2_1/c$; Ln = Pr (**VI**), Nd (**VII**), Sm (**VIII**)} and $[Ln(pdc)(H_2O)_4]_3 \cdot 3Cl$ {$Ia\bar{3}$; Ln = Sm (I**X**), Eu (**X**)}.

2.2.3 Single crystal structure determination

Full crystallographic data sets of **I**-**V** were collected at 296(2) *K* using a Bruker D8 QUEST CMOS diffractometer operated with graphite-monochromated Mo K_α radiation (λ = 0.71073 Å), and those of **VI**-**X** were collected at 298(2) *K* (except for **VIII** at 273(2) *K*) using a Bruker D8 Venture diffractometer (Photon CMOS detector) operated with a micro focus sealed tube X-ray source with graphite monochromatic Mo K_α radiation (λ = 0.71073 Å). All structures were solved by direct methods using the SHELXS program [13] and refined on F^2 by the full-matrix least squares technique using the SHELXL program [13] *via* the Olex2 interface [14]. Empirical absorption corrections were applied to all data using the SADABS program [15].

In order to take the contribution of the disordered chloride anions into account in the cases of **I**-**V**, the SQUEEZE option provided in the program PLATON [16] was achieved after two chloride anions were located in every structure. Numbers of electrons per unit cell to be found in the framework accessible voids were determined, and numbers of equivalent chloride anions were calculated: 10 (**I** and **IV**), 9 (**II** and **III**) and 7 (**V**) chlorides per unit cell, which led to the addition of one chloride per formula that is chemically sensible. Similar treatment was also required for **VI**-**X.** In case of **VI** and **VII**, numbers of equivalent water molecules were calculated: 10 (**VI**) and 5 (**VII**) crystallized water molecules per unit cell. These values led to the addition of one crystallized water per formula. In the cases of **VIII**-**X**, 9 chlorides per unit cell was calculated leading to one chloride per formula. The application of SQUEEZE on these structures resulted in significant improvement of the *R* and *Rw* values as shown in Table 2.1. There is additional site disordering at the chloride anion in every structure possessing the chloride as guest anions. Appreciable improvement in the final residual electron density maxima and minima was achieved after the treatment of such. The crystallographic and refinement data of **I**-**X** are summarized in Table 2.1.

2.2.4 Thermogravimetric studies of V and VI

Since only complexes **V** ($Pa\bar{3}$) and **VI** ($P2_1/c$) could be obtained with high purity, thermogravimetric analysis of **V** was performed on a Perkin Elmer Pyris Diamond TG/DTA from 35 ˚C to 1100 ˚C with a heating rate 10 ˚C·min^{-1} in a nitrogen gas flow.

The experiment on crystals of **VI** was carried on using a Linseis TG/DTA with a STA PT1600 model and the temperature range of 27-1000 ˚C with a heating rate 10 ˚C·min^{-1} in a nitrogen gas flow.

2.2.5 Hirshfeld surface analysis

Hirshfeld surface analysis has recently become a well-known method for visualizing and exploring significant close contacts and intermolecular interactions in molecular crystals [17-19]. Since this method can identify the interactions within the context of whole system, details regarding molecular packing, polymorphism, and supramolecular arrangement can be investigated [20,21]. 3D Hirshfeld surface maps are generated with the normalized contact distance (d_{norm}) using a red-white-blue color scheme, indicating shorter contacts, van der Waal (vdW) contacts and longer contacts, respectively. All contact distances to the Hirshfeld surface, such as internal distances (d_i) and external distances (d_e), can be illustrated in the 2D fingerprint plots, and their contributions can be exhibited in terms of a percentage share [22].

Here, the 3D Hirshfeld surface and 2D fingerprint calculations were adopted for the analysis of intermolecular interactions in **VI-VIII** using the Crystal Explorer [23]. Based on the standard neutron H–X bond lengths (C–H = 1.083 Å, O–H = 0.983 Å, N–H = 1.009 Å), the 3D Hirshfeld surfaces were constructed using high resolution and mapped with the d_{norm} functions. 2D fingerprint plots were generated with the use of also the same software.

2.3 Results and discussion

2.3.1 Influences of heating techniques on crystal structures

Although the synthesis of the materials using two different heating techniques, *i.e*. the microwave heating and the heating under reflux or commonly called the conventional heating, led to crystals of similar habits under an optical microscope, there was significant distinction in the molecular details of the products. After evaporation of the solvent, the product crystals yielded from both synthetic techniques were apparent with colors of the corresponding Ln^{III} ions. According to the single-crystal X-ray diffraction results, five new isostructural complexes **I-V** crystallizing in the cubic $Pa\bar{3}$ space group were obtained

Table 2.1 Crystallographic data and refinement details for **I-X**.

	I	**II**	**III**	**IV**	**V**
CCDC No.	1448352	1448353	1448354	1494337	1494338
Formula[a]	$C_{21}H_{33}N_3O_{24}Cl_3Pr_3$	$C_{21}H_{33}N_3O_{24}Cl_3Nd_3$	$C_{21}H_{33}N_3O_{24}Cl_3Sm_3$	$C_{21}H_{33}N_3O_{24}Cl_3Eu_3$	$C_{21}H_{33}N_3O_{24}Cl_3Gd_3$
Formula weight[a]	1240.57	1250.57	1268.93	1273.74	1289.60
Temperature (K)	296(2)	296(2)	296(2)	296(2)	296(2)
Crystal system	Cubic	Cubic	Cubic	Cubic	Cubic
Space group	$Pa\bar{3}$ (No. 205)	$Pa\bar{3}$ (No. 205)	$Pa\bar{3}$ (No. 205)	$Pa\bar{3}$ (No. 205)	$Pa\bar{3}$ (No. 205)
a (Å)	19.9853(3)	19.9091(6)	19.8330(3)	19.8085(6)	19.7822(6)
V (Å)3	7982.4(4)	7891.4(4)	7801.3(4)	7772.4(4)	7741.5(4)
Z	8	8	8	8	8
F(000)	4664	4688	4736	4760	4784
ρ (mg·m^{-3})	2.006	2.046	2.100	2.121	2.152
μ (mm^{-1})	3.824	4.112	4.682	5.008	5.307
Data/Restraints/Parameters	4283/6/168	3268/0/168	3966/12/170	2997/0/168	2953/0/168
GOOF	1.104	1.153	1.098	1.187	1.199
Before SQUEEZE					
R_1 ($I=2\sigma(I)$)[b]	0.0490	0.0470	0.0569	0.0598	0.0404
wR_2 (all data)[b]	0.1419	0.1433	0.1701	0.1542	0.1116
After SQUEEZE					
R_1 ($I=2\sigma(I)$)[b]	0.0383	0.0293	0.0389	0.0555	0.0325
wR_2 (all data)[b]	0.0686	0.0627	0.0739	0.0703	0.0565

[a]Include one chlorine atom approximated using SQUEEZE. [b]$R_1 = \Sigma||F_0|-|F_c||/|F_0|$, $wR_2 = [\Sigma w(F_0^2-F_c^2)^2/\Sigma w(F_0^2)_2]^{1/2}$.

Table 2.1 Crystallographic data and refinement details for **I-X** (continued).

	VI	**VII**	**VIII**	**IX**	**X**
CCDC No.	1494339	1494340	1494342	1494341	1494343
Formula[a]	$C_{14}H_{14}N_2O_{12}Pr$	$C_{14}H_{14}N_2O_{12}Nd$	$C_{14}H_{19}N_2O_{14}Sm$	$C_{21}H_{33}Cl_2N_3O_{24}Sm_3$	$C_{21}H_{33}Cl_2N_3O_{24}Eu_3$
Formula weight[a]	543.18	546.51	589.66	1233.48	1238.28
Temperature (*K*)	298(2)	298(2)	273(2)	298(2)	298(2)
Crystal system	monoclinic	monoclinic	monoclinic	cubic	cubic
Space group	$P2_1/c$ (No. 14)	$P2_1/c$ (No. 14)	$P2_1/c$ (No. 14)	$Ia\bar{3}$ (No. 206)	$Ia\bar{3}$ (No. 206)
a (Å)	14.785(3)	14.810(3)	13.9892(5)	19.8346(9)	19.8027(10)
b (Å)	10.9727(18)	11.064(2)	11.2046(3)	-	-
c (Å)	12.936(2)	12.944(3)	12.8312(3)	-	-
α (°)	90.00	90.00(3)	90.00	90.00	90.00
β (°)	100.256(6)	100.23(3)	102.314(2)	90.00	90.00
γ (°)	90.00	90.00(3)	90.00	90.00	90.00
V (Å)^3	2065.0(6)	2087.4(7)	1964.93(10)	7803.2(6)	7765.6(7)
Z	4	4	4	8	8
F(000)	1068.0	1072.0	1164.0	4736.0	4760.0
ρ (mg·m^{-3})	1.747	1.739	1.993	2.100	2.118
μ (mm^{-1})	2.421	2.548	3.067	4.681	5.013
Data/Restraints/Parameters	9145/0/270	7906/0/270	4897/0/294	2841/0/88	3670/2/88
GOOF	1.049	1.038	1.096	1.194	1.177
Before SQUEEZE					
R_1 (I=2σ(I))[b]	0.1407	0.1924	0.0467	0.0720	0.1050
wR_2 (all data)[b]	0.2963	0.2369	0.0799	0.1488	0.1506
After SQUEEZE					
R_1 (I=2σ(I))[b]	0.0836	0.0719	0.0339	0.0532	0.0649
wR_2 (all data)[b]	0.2346	0.1762	0.0799	0.1075	0.1089

[a]Include one chlorine atom approximated using SQUEEZE. [b]$R_1 = \Sigma||F_0|-|F_c||/|F_0|$, $wR_2 = [\Sigma w(F_0^2-F_c^2)^2/\Sigma w(F_0^2)^2$

from the microwave heating method. These complexes are also isostructural with the previously reported complex ($[La(pdc)(H_2O)_4]_3 \cdot 3Cl$) [24]. From the PXRD patterns collected on bulk products obtained from microwave synthesis (Fig. 2.2), there are however peaks mismatched with the corresponding diffractions generated from the single crystal data. The conventional heating technique however provided five other different complexes **VI**-**X** in accordance with the single-crystal X-ray diffraction results. Among them, three isostructural complexes **VI**-**VIII** crystallizing in the monoclinic $P2_1/c$ space group are also isostructural to the complexes yielded by hydrothermal method [25,26]. The other two isostructural complexes **IX** and **X** crystallizing in the cubic $Ia\bar{3}$ space group are notably new. Nevertheless, if the PXRD patterns collected on bulk samples synthesized by conventional heating (Fig. 2.2) are closely considered, the yielded product can be classified into three groups of isostructural crystals (Fig. 2.1): (i) the monoclinic $P2_1/c$ structures **VI** (Pr), **VII** (Nd), and **VIII** (Sm), (ii) the cubic $Ia\bar{3}$ structures **IX** (Sm), and **X** (Eu), and (iii) the cubic $Pa\bar{3}$ structures **II** (Nd), **III** (Sm), **IV** (Eu), and **V** (Gd). Besides, there are a few key observations. First, only the monoclinic $P2_1/c$ (**VI**, Pr) and the cubic $Pa\bar{3}$ (**V**, Gd) structures can be yielded as pure phases upon being synthesized by the conventional heating. Second, the crystal symmetry of the products has a tendency to increase across the Ln series, that is from the pure monoclinic $P2_1/c$ in Pr (**VI**) to the mix of the monoclinic $P2_1/c$ and the cubic $Pa\bar{3}$ and $Ia\bar{3}$ in Nd (**II**+**VII**) and Sm (**III**+**VIII**+**IX**), to the mix of cubic $Pa\bar{3}$ and $Ia\bar{3}$ in Eu (**IV**+**X**), and to the pure cubic $Pa\bar{3}$ in Gd (**V**). Third, the cubic $Ia\bar{3}$ structures **IX** and **X** are the supramolecular isomers of the cubic $Pa\bar{3}$ structures **III** and **IV**, respectively. Forth, the cubic structures are more favorable than the monoclinic in both heating techniques with the exception of the Pr complexes.

Since the crystals were grown after the evaporation of the ethanol solvent in every case, this suggests the nucleation process to be critical in determining the final structures. According to the literature discussing the nucleation process for the microwave synthesis [27], the nucleation process is kinetically controlled. Since the cubic $Pa\bar{3}$ structures are always obtained from the microwave synthesis independent on type of the Ln^{III} ions, therefore it can be concluded that the cubic $Pa\bar{3}$ structures are favored kinetically. However, the conventional heating which provides thermodynamically favorable structures leads to the structures with different symmetries and supramolecular

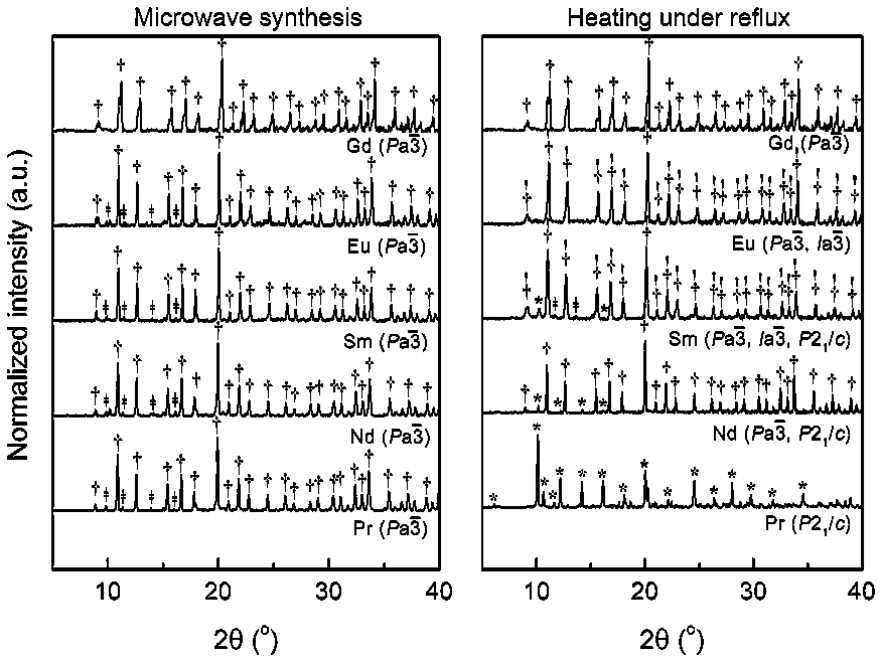

Fig. 2.2 Experimental PXRD patterns of bulk solids obtained from the microwave synthesis (left) and the heating under reflux (right). The symbols indicate the difference in space groups as follows; † ($Pa\bar{3}$), ˡ ($Ia\bar{3}$), * ($P2_1/c$), ǂ (unknown).

assemblies. These structures should therefore be favored thermodynamically. In addition, since the cubic $Pa\bar{3}$ structures are yielded in every synthesis except for the Pr case (**VI**), this suggests that the cubic $Pa\bar{3}$ structures should be favored in both kinetic and thermodynamic points of view.

The change in crystal structures with type of the Ln^{III} ions in the case of conventional heating can be due to the different numbers of coordinating organic ligands that can be accommodated by the Ln^{III} ions. The Pr^{III} ion with relatively large ionic radius can accommodate more organic ligands in comparison with the other smaller Ln^{III} ions. Different numbers of coordinating water molecules which depend on the hydration enthalpies of the Ln^{III} ions may also be the reason. In the case of complex **VI**, the Pr^{III} ion holding the lowest hydration energy can occupy only two water molecules in its coordination sphere. As for the heavier Ln^{III} ions possessing higher hydration energy, there are four coordinating water molecules. These reasons lead to the Ln^{III} : pdc^{2-}/$Hpdc^{-}$: H_2O_{ligand} ratios of 1 : 2 : 2 in the monoclinic structures **VI**-**VIII** compared with 1 : 1 : 4 in the cubic structures **I**-**V**, **IX** and **X**. Similar structural variation from cubic to

monoclinic structures has been reported for $[La(pdc)(H_2O)_4]_3 \cdot 3Cl$ [24]. The cubic $Pa\bar{3}$ $[La(pdc)(H_2O)_4]_3 \cdot 3Cl$ structure was altered to the monoclinic $P2_1/c$ ladder-like $[La(pdc)(Hpdc)(H_2O)_2] \cdot 3H_2O$ by using a stoichiometric amount of $AgBF_4$ [24].

2.3.2 Crystal structure description of I-X

The cubic $Pa\bar{3}$ structures: $[Ln(pdc)(H_2O)_4]_3 \cdot 3Cl$ (I-V). After the employment of SQUEEZE application dealing with the undefined chloride anions, complexes **I-V** are revealed to be isostructural with the previously reported $[La(pdc)(H_2O)_4]_3 \cdot 3Cl$ [24]. They crystallize in the cubic $Pa\bar{3}$ space group with cell parameter *a* and *V* decreasing from **I** (Pr) to **V** (Gd) (Table 2.1), which is consistent with the lanthanide contraction [28]. The extended asymmetric unit including the unbound chloride anions of **I** as the representative complex for **I**, **II**, **IV** and **V** and that of **III** are shown in Fig. 2.3. In complexes **I-V**, each Ln^{III} ion is coordinated to one nitrogen atom (N1) and two oxygen atoms (O1 and O3) from the chelating pdc^{2-} ligand, two oxygen atoms (O2 and O4) from two different bridging pdc^{2-} ligands, and four oxygen atoms (O5-O8) from four coordinated water molecules. These coordinating atoms lineate the square-face monocapped antiprismatic geometry about the Ln^{III} ions, *SAPRS*-$\{LnO_8N\}$ (Fig. 2.3c).

Two additional chloride anions (Cl1 and Cl2) are also included in the asymmetric units of all complexes. One of the chloride anions (Cl2) in every structure (Fig. 2.3a), except **III**, shows additional disorder over two crystallographic sites with different site occupancy Cl2A : Cl2B ratios; 0.932 : 0.068 for **I**, 0.605 : 0.395 for **II**, 0.582 : 0.418 for **IV**, and 0.719 : 0.281 for **V**. For complex **III**, the chloride ion (Cl2) exhibits similar disorder but over three crystallographic sites (Fig. 2.3b) with site occupancy Cl2A : Cl2B : Cl2C ratio of 0.40 : 0.55: 0.05. The bond valence sum (BVS) calculations based on the Ln–O and Ln–N distances confirm the trivalent state of the Ln^{III} ions. Each pdc^{2-} ligand connecting to three Ln^{III} ions exhibits the common chelating mode of coordination, using the pyridyl N atom and two carboxylate μ_2-η^1:η^1 O atoms as shown in Fig. 2.3d. The coordination as described results in almost complete co-planarity between the carboxylate groups and the central pyridyl ring. The Ln–O and Ln–N bond distances of the complexes **I-V** are in good agreement with those of the reported $[La(pdc)(H_2O)_4]_3 \cdot 3Cl$ structure [24].

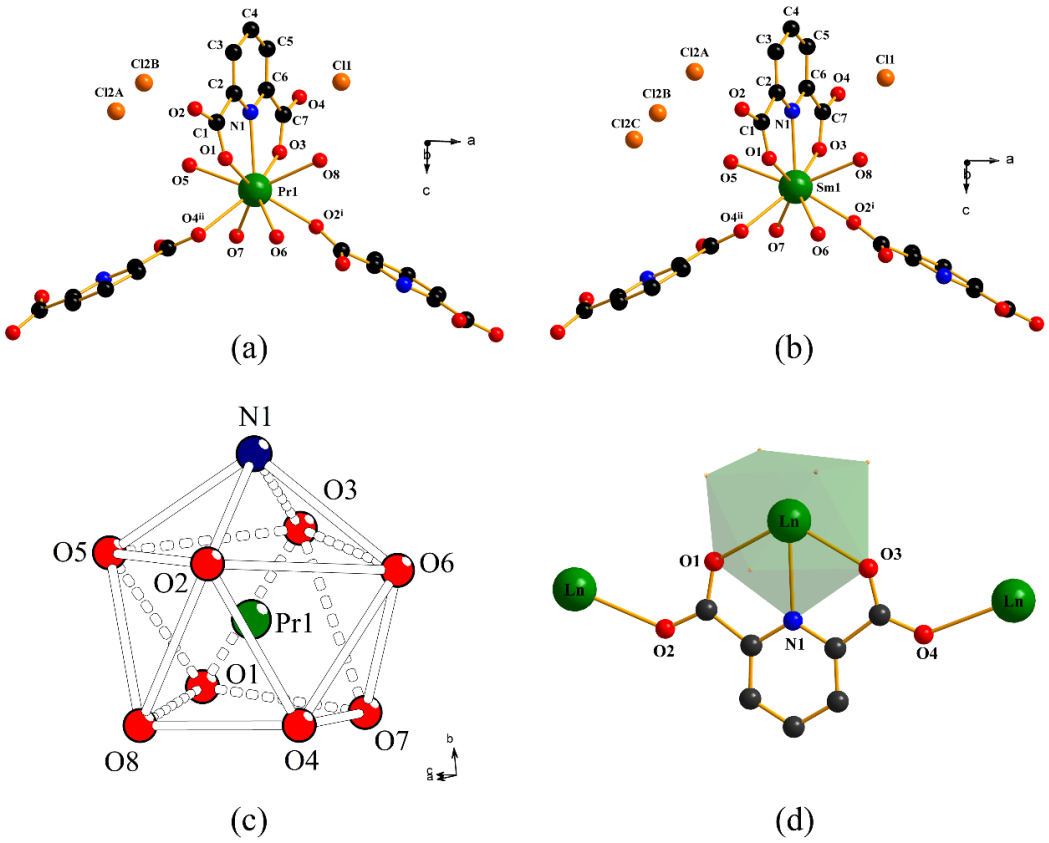

Fig. 2.3 Illustrations showing (a) extended asymmetric unit of **I** and (b) **III**, (c) the *SAPRS*-{PrO_8N} unit, and (d) the coordination mode of pdc^{2-} ligand. Hydrogen atoms are omitted for clarity. Symmetry codes: (i) *x*, 1.5-*y*, 0.5+*z*; (ii) 1-*x*, 1-*y*, 1-*z*.

The 3D infinite frameworks of **I-V** are built up of the discrete *SAPRS*-{LnO_8N} units each of which is linked to four adjacent units through three pdc^{2-} linkers. This four-connection manner is manifested to be a distorted seesaw shape as shown in Fig. 2.4a. The further linkage of the *SAPRS*-{PrO_8N} units leads to the formation of a hexagonal ring of chair conformation (Fig. 2.4b) and successively the establishment of the discrete 1D channels extending in four <1 1 1> directions along the 3-fold rotoinversion axes (Fig. 2.4c). The channel openings range from 2.96(1) Å to 3.35(3) Å. The interior surface of these channels is decorated with the coordinated water molecules and is therefore hydrophilic in nature. Inside these channels, there are unbound chloride anions which are transfixed by the coordinated water molecules through the hydrogen bonding interactions (Fig. 2.4d).

The appearance of these chloride anions also plays an important role in balancing the positive charge of the tubular frameworks. The O–H···Cl hydrogen bonding interactions which are related to the existence of every chloride anions including the disorder chlorides located at the center of the channels, as well as the O–H···O interactions are tabulated in Table 2.2.

The cubic $Ia\bar{3}$ structures: $[Ln(pdc)(H_2O)_4]_3 \cdot 3Cl$ (IX-X). After the use of SQUEEZE application to treat the disordered chloride anions, complexes **IX** and **X** are revealed to be the supramolecular isomers of complexes **III** and **IV**, respectively. The asymmetric units of these complexes comprise one unique Ln^{III} ion, half a molecule of the fully deprotonated pdc^{2-} ligand, two coordinated water molecules and one chloride anion which exhibits positional disorder over two crystallographic sites (Cl1A and Cl1B). The occupancy ratios of Cl1A:Cl1B in both structures are very similar; that is, 0.256(11) : 0.744(11) for **IX**, and 0.262(9) : 0.738(9) for **X**. The Ln–N and Ln–O distances observed in these complexes are very similar to those observed in the corresponding isomers and are also in good agreement with those of the previously reported $[La(pdc)(H_2O)_4]_3 \cdot 3Cl$ structure [24]. The extended asymmetric unit of **IX** and **X** which is closely similar to the corresponding isomers is shown in Fig. 2.5a and Fig. 2.5b, respectively.

Because complexes **IX** and **X** are the isomers of complexes **III** and **IV**, the coordination environment about the Ln^{III} ion and mode of coordination adopted by the pdc^{2-} ligand are principally identical. However, if conformation of the linkages between each *SAPRS*-$\{LnO_8N\}$ unit in the structures is carefully considered, the arrangement of the *SAPRS*-$\{LnO_8N\}$ units in **IX** and **X** is not exactly same as those of **III** and **IV**, respectively, but they are enantiomers to each other (Fig. 2.5c). The arrangement of the linkage between the *SAPRS*-$\{LnO_8N\}$ unit and the bridging pdc^{2-} ligands in the cubic $Pa\bar{3}$ complexes (**III** and **IV**) is found to be the Λ stereoisomer, whereas the arrangement of those in the cubic $Ia\bar{3}$ complexes (**IX** and **X**) is the enantiomeric counterpart, Δ.

The formation of the 3D frameworks and the occluded 1D channels in complexes **IX** and **X** is closely similar to those of complexes **I-V**. The unbound chloride anions are inhabited at the center of the channels that are coincident with the 3-fold rotoinversion axes. The O–H···Cl hydrogen bonding interactions which are related to the existence of every disorder chlorides at the center of the channels, as well as the O–H···O interactions

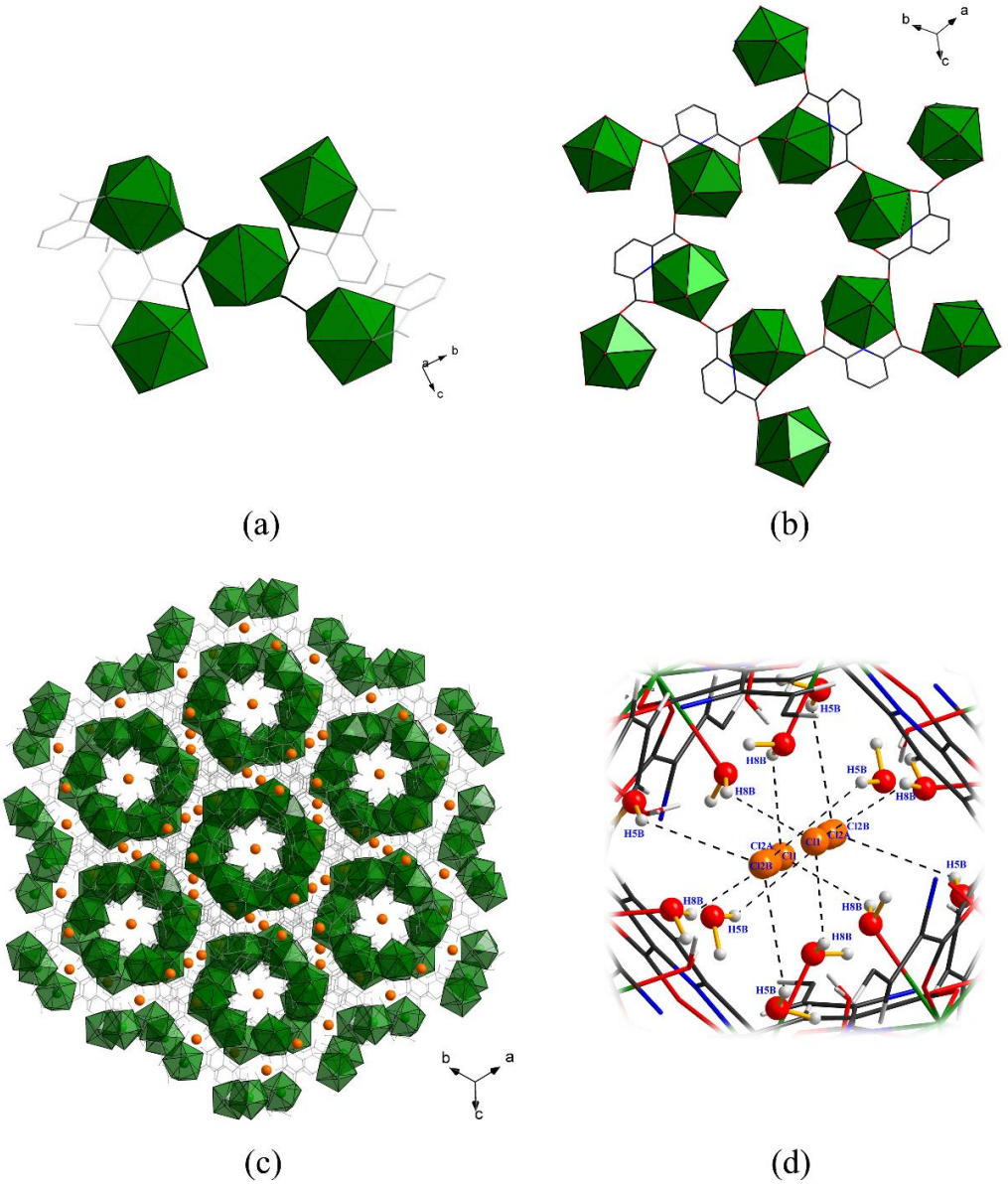

Fig. 2.4 Perspective views of (a) the linkage of four-connected polyhedral, (b) a carboxylate bridged hexagonal ring, (c) the infinite tubular structure of **I** (as representative of **I**-**V** and **IX**-**X**), and (d) hydrogen bonding interactions of chloride anions and coordinated water molecules.

observed in the tubular structures of **IX** and **X** are listed in Table 2.2. The existence of the chloride anions which align along the directions of the channels *via* the hydrogen bonding interactions with coordinated water molecules is an important factor in the construction of the tabular frameworks in the cubic $Pa\bar{3}$ and $Ia\bar{3}$ complexes.

Table 1.2 Hydrogen bonding geometries for **I-X**.

I[a]			**II**[b]		
D–H···A	D···A	∠D–H···A	D–H···A	D···A	∠D–H···A
O5–H5A···O2^{i}	3.171(8)	145	O5–H5A···O3^{i}	2.931(2)	147
O5–H5A···O3^{ii}	2.874(7)	132	O5–H5B···Cl2A^{ii}	3.084(8)	140
O5–H5B···Cl2A	3.141(2)	82	O5–H5B···Cl2B	3.281(7)	122
O5–H5B···Cl2B	3.142(2)	111	O6–H6B···O3^{i}	2.687(7)	151
O6–H6A···O1^{iii}	2.640(1)	160	O7–H7B···O1^{iii}	2.650(7)	154
O8–H8B···Cl1	3.113(1)	131	O8–H8B···Cl1	3.120(4)	97
			O8–H8B···Cl2A	3.481(3)	127
III[c]			**IV**[d]		
D–H···A	D···A	∠D–H···A	D–H···A	D···A	∠D–H···A
O5–H5A···Cl2A	3.260(7)	132	O5–H5B···Cl1	3.136(5)	134
O5–H5A···Cl2B^{i}	3.055(6)	133	O6–H6A···O3^{i}	2.689(2)	153
O5–H5B···O3^{ii}	2.941(4)	144	O7–H7B···O1^{ii}	2.637(3)	160
O6–H6A···O1^{iii}	2.638(7)	157	O8–H8A···Cl2A^{iii}	3.053(8)	133
O7–H7B···O3^{ii}	2.675(5)	138	O8–H8A···Cl2B	3.242(9)	136
O8–H8A···Cl2C	2.750(3)	85	O8–H8B···O3^{i}	2.929(1)	140
O8–H8B···Cl1	3.131(5)	119			
V[e]			**VI**[f]		
D–H···A	D···A	∠D–H···A	D–H···A	D···A	∠D–H···A
O5–H5A···Cl2A	3.476(3)	149	O9–H9A···O2^{i}	2.7734	153
O5–H5B···Cl1	3.123(8)	145	O9–H9B···O7^{ii}	2.7805	158
O6–H6B···O1^{i}	2.634(8)	161	O10–H10A···O12^{iii}	2.8298	157
O7–H7B···O3^{ii}	2.681(9)	158	O10–H10B···O11^{iv}	2.6474	114
O8–H8A···O3^{ii}	2.902(3)	151	O11–H11A···O12	2.9134	155
O8–H8B···Cl2A^{iii}	3.106(8)	139	O11–H11B···O6	2.7336	152
O8–H8B···Cl2B	3.271(9)	124	O12–H12A···O5	2.9376	173
			O12–H12B···O6	2.8747	154
VII[g]			**VIII**[h]		
D–H···A	D···A	∠D–H···A	D–H···A	D···A	∠D–H···A
O9–H9A···O4^{i}	2.7863	109	O9–H9A···O11^{i}	2.7391	151
O9–H9B···O7^{ii}	2.7757	156	O9–H9B···O12^{ii}	2.7146	123
O10–H10A···O11^{iii}	2.8071	149	O10–H10A···O2^{iii}	2.7163	124
O10–H10B···O12^{iv}	2.7014	108	O10–H10B···O7^{iv}	2.7202	148
O11–H11A···O6^{iv}	2.9200	164	O11–H11A···O6^{ii}	2.8753	171
O11–H11B···O5	2.9442	156	O11–H11B···O5	2.9192	165
O12–H12A···O11	2.9177	159	O12–H12A···O6	2.6863	173
O12–H12B···O6	2.7435	148	O12–H12B···O11	2.9044	146
			O13–H13A···O12	3.0067	131
			O14–H14A···O13^{v}	2.7919	134
			O14–H14B···O2^{iii}	2.6354	163
IX[i]			**X**[j]		
D–H···A	D···A	∠D–H···A	D–H···A	D···A	∠D–H···A
O3–H3A···O1^{i}	3.0782	118	O3–H3A···O1^{i}	3.0821	109
O3–H3B···Cl1B	3.1946	142	O3–H3B···Cl1B^{ii}	3.1894	150
O4–H4A···O1^{i}	2.6478	135	O4–H4B···O1^{iii}	2.6539	151

[a] Symmetry codes: (i) = -0.5+*x*, 0.5-*y*, 1-*z*; (ii) = 0.5-*x*, 0.5+*y*, *z*; (iii) = -0.5+*x*, *y*, 0.5-*z*
[b] Symmetry codes: (i) = 0.5-*x*, 0.5+*y*, *z*; (ii) = 0.5+*x*, *y*, 0.5-*z*; (iii) = -0.5+*x*, *y*, 0.5-*z*
[c] Symmetry codes: (i) = 0.5+*x*, *y*, 0.5-*z*; (ii) = 0.5-*x*, 0.5+*y*, *z*; (iii) = -0.5+*x*, *y*, 0.5-*z*
[d] Symmetry codes: (i) = 0.5-*x*, 0.5+*y*, *z*; (ii) = -0.5+*x*, *y*, 0.5-*z*; (iii) = 0.5+*x*, *y*, 0.5-*z*
[e] Symmetry codes: (i) = *x*, 0.5-*y*, -0.5+*z*; (ii) = 0.5+*x*, *y*, 0.5-*z*; (iii) = *x*, 0.5-*y*, 0.5+*z*
[f] Symmetry codes: (i) = 1-*x*, 0.5+*y*, 0.5-*z;* (ii) = *x*, 0.5-*y*, 0.5+*z;* (iii) = *x*, 0.5-*y*, -0.5+*z*; (iv) = -*x*, -0.5+*y*, 0.5-*z*.
[g] Symmetry codes: (i) = 1-*x*, 0.5+*y*, 0.5-*z;* (ii) = *x*, 0.5-*y*, 1/2+*z;* (iii) = *x*, 0.5-*y*, -0.5+*z;* (iv) = -*x*, -0.5+*y*, 0.5-*z*.
[h] Symmetry codes: (i) = *x*, 0.5-*y*, -1/2+*z*; (ii) = -*x*, -0.5+*y*, 0.5-*z*; (iii) = 1-*x*, 0.5+*y*, 0.5-*z*; (iv) = *x*, 0.5-*y*, 0.5+*z*; (v) = 1-*x*, 1-*y*, 1-*z*.
[i] Symmetry codes: (i) = 2/1-*x*,2/1 -*y*, 2/1-*z*.
[j] Symmetry codes: (i) = *x*,2/1 -*y*, -2/1+*z*; (ii) = *x*, -*y*, 1/2-*z*; (iii) = 1/2-*x*, 1/2-*y*, 1/2-*z*.

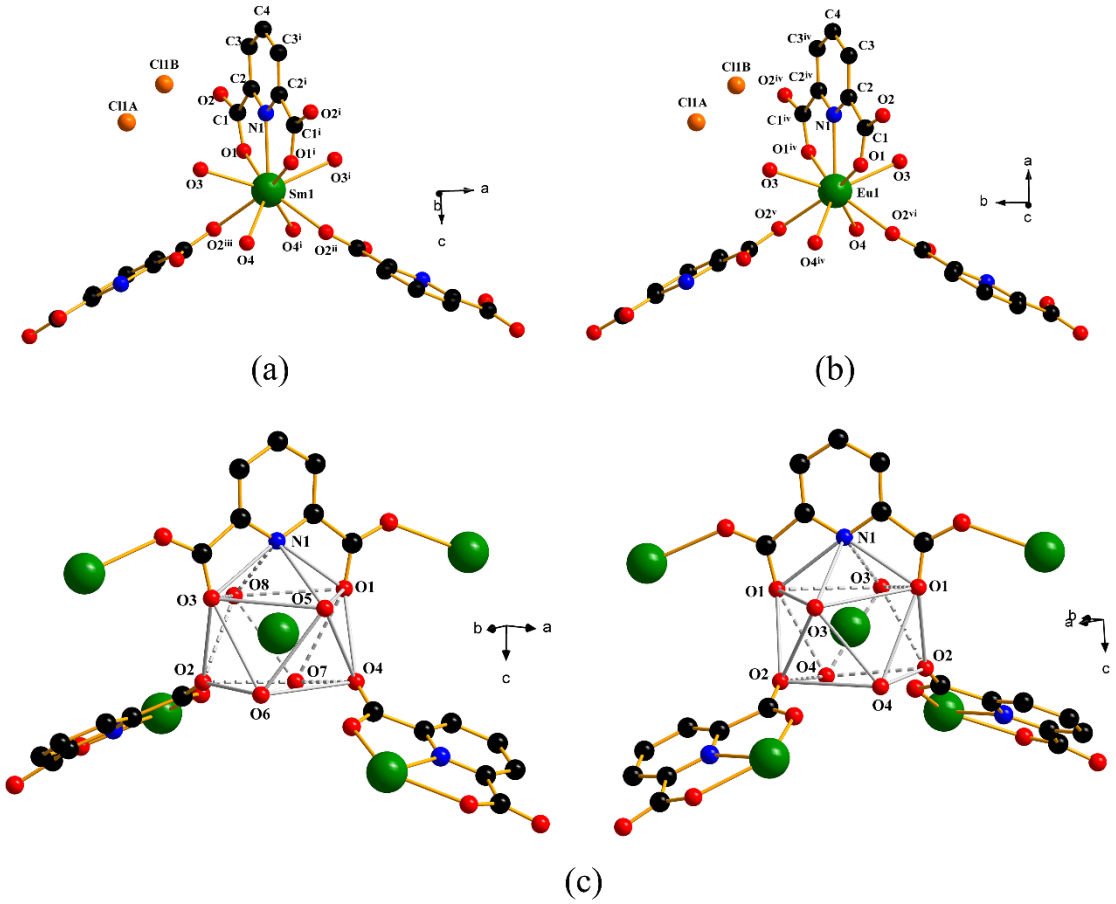

Fig. **2.5** Illustrations showing (a) an extended asymmetric unit of **IX**, (b) the extended asymmetric unit of **X**, and (c) the enantiomeric Λ (left: **III** and **IV**) and Δ (right: **IX** and **X**) configurations. Hydrogen atoms are omitted for clarity. Symmetry codes: (i) 1-*x*, 1.5-*y*, *z*; (ii) 0.5+*x*, *y*, 1.5-*z*; (iii) 0.5+*x*, 1-*y*, *z*; (iv) *x*, 1-*y*, 0.5-*z*; (v) 1-*x*, 1-*y*, 1-*z*; (vi) -0.5+*x*, 1-*y*, *z*.

Topological studies of both cubic $Pa\bar{3}$ and $Ia\bar{3}$ structures were performed with the help of TOPOSPRO 5.0 program package [29]. Although there are the different sets of symmetry operations and the Wyckoff positions adopted by the $Pa\bar{3}$ and the $Ia\bar{3}$ structures, topological nets constructed from these cubic structures with two different space groups are identical. The $Pa\bar{3}$ (**I**-**V**) and $Ia\bar{3}$ (**IX**-**X**) structures can be simplified into the interpenetrated net of the unimodal **lcs** and **pcu** nets (Fig. 2.6). If the hydrogen bonding interactions between chloride anions and coordinated water molecules is disregarded, the *SAPRS*-{LnO_8N} unit can be simplified as node which is connected to one another leading to the formation of a unimodal 4-connected **lcs** net with $\{6^6\}$ point

symbol. On the other hand, if only $\{Cl_2(H_2O)_6\}$ units are taken as nodes, the unimodal 6-connected **pcu** net with $\{4^{12}.6^3\}$ point symbol is obtained. The interpenetration of these two nets forms the network in **I-V** and **IX-X**.

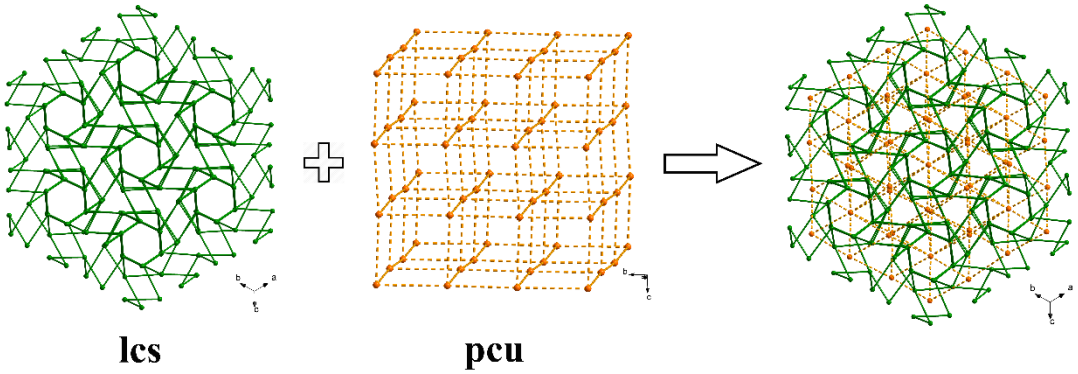

Fig. 2.6 Illustration of the interpenetrated unimodal **lcs** and **pcu** nets in the cubic structures.

The monoclinic $P2_1/c$ structures: $[Ln(pdc)(Hpdc)(H_2O)_2]\cdot 3H_2O$ (VI-VIII). The monoclinic complexes **VI-VIII** were obtained only from the heating under reflux. The bulk products of **VII** (Nd) and **VIII** (Sm) were revealed to be associated with the other higher symmetric phases such as the cubic $Pa\bar{3}$ for Nd complex and the cubic $Pa\bar{3}$ and $Ia\bar{3}$ for Sm complex according to the PXRD patterns (Fig. 2.2). However, the Pr complex (**VI**) could be obtained as the pure monoclinic $P2_1/c$ phase. The cubic $Pa\bar{3}$ phase is apparently favored for the other Ln^{III} ions. These $P2_1/c$ complexes have been reported to be yielded also from the hydrothermal syntheses [25, 26]. In complexes **VI-VIII**, each Ln^{III} ion is nine-fold coordinated to one nitrogen atom (N1) and two oxygen atoms (O1 and O3) from one partially deprotonated $Hpdc^-$ ligand, one nitrogen atom (N2) and two oxygen atoms (O5 and O7) from one fully deprotonated pdc^{2-} ligand, one additional oxygen atom (O8) from the other fully deprotonated pdc^{2-} ligand, and two oxygen atoms (O9 and O10) from two coordinated water molecules. There are additional two water molecules of crystallization included in the asymmetric units except for **VIII** which has four water molecules of crystallization. The extended asymmetric units of **VI-VIII** are shown in Fig. 2.7 with the atomic numbering scheme. It is however noted that the protonated H atom of $Hpdc^-$ in **VIII** could not be located in the electron density map. The nine-fold coordination about the Ln center leads to the formation of *SAPRS*-$\{LnO_7N_2\}$

unit which is similar to that found in the other cubic structures, except that they are highly distorted (Fig. 2.8a). Unlike the cubic structures, the monoclinic structures are not only composed of the partially deprotonated $Hpdc^-$ ligand and have less coordinated water molecules, but there are also two different coordination modes of the ligands owing to their different degrees of deprotonation. The pdc^{2-} ligand coordinates to two Ln^{III} ions through the pyridyl N atom (N2) and the μ_1-η^1:η^0 (O5) and μ_2-η^1:η^1 (O7, O8) carboxylate groups (Fig. 2.8b). The $Hpdc^-$ ligand, on the other hand, connects to the Ln^{III} ion through the pyridyl N atom (N1), the deprotonated μ_1-η^1:η^0 (O3) carboxylate group and the protonated μ_1-η^1:η^0 (O1) carboxylate group (Fig. 2.8c). The Ln–O and Ln–N bond distances of the complexes **VI-VIII** are in good agreement with those of the previously reported $[Ln(pdc)(Hpdc)(H_2O)_2]\cdot 3H_2O$ [25,26].

The discrete *SAPRS*-$\{LnO_7N_2\}$ unit is linked to the adjacent equivalents by the oxygen atoms (O8) from the pdc^{2-} ligands leading to the formation of an infinite 1D $[Ln(pdc)(Hpdc)(H_2O)_2]$ chain extending along the *c* axis (Fig. 2.9a). Because of the anti-parallel arrangement between the $Hpdc^-$ and pdc^{2-} ligands in each unit, the 1D chain features a zigzag chain rather than being straight. In contrast to the cubic structures, the presence of the $Hpdc^-$ ligand in these monoclinic structures hinders the linkage of the adjacent Ln^{III} ions to form higher dimensional coordination framework. These chains are assembled however *via* the hydrogen bonding interactions between the coordinated water molecules and the oxygen atoms (O2) from the $Hpdc^-$ ligands leading to a ladder-like band extending along also the direction of *c* axis (Fig. 2.9b). According to the statistics on the structures submitted to the Cambridge Structural Database (CSD) [3], the $Hpdc^-$ ligand is liable to participate in the creation of the ladder-like fashion in both monoclinic $P2_1/c$ and $P2_1/a$ space groups [4-6,30]. The ladder-like bands are further assembled to one another by free water molecules through the hydrogen bonding interactions resulting in the generation of 2D supramolecular sheet expanding along the *ac* plane (Fig. 2.9c). Likewise, the free water molecules also link 2D sheets *via* the hydrogen bonding interactions which are clearly seen in the *ab* plane and eventually lead to the establishment of 3D supramolecular network (Fig. 2.10). The lists of hydrogen bonding interactions in **VI-VIII** are tabulated in Table 2.2.

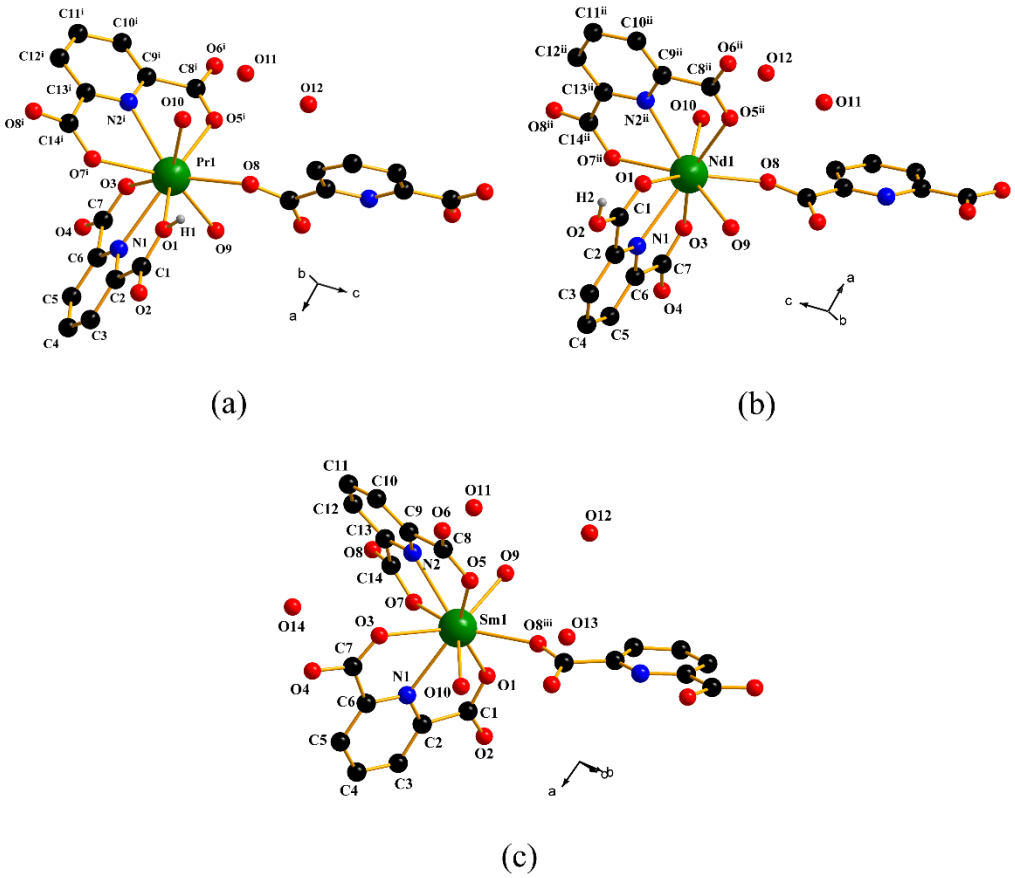

Fig. 2.7 The extended asymmetric units of **VI** (a), **VII** (b), and **VIII** (c). Hydrogen atoms are omitted for clarity except for those protonated ones. Symmetry codes: (i) *x*, 0.5-*y*, -0.5+*z*; (ii) *x*, 1.5-*y*, 0.5+*z*; (iii) *x*, 0.5-*y*, 0.5+*z*.

2.3.3 Hirshfeld surface analysis of the monoclinic complexes VI-VIII

The supramolecular arrangement of the 1D chains in the crystal structures of **VI-VIII** is mainly dominated by the O–H···O hydrogen bonding interactions. As the 3D Hirshfeld surface of the selected region in 1D chain of **VI** (as a representative of **VII** and **VIII**) was generated using the d_{norm} function, several red spots appeared suggesting the close contacts of intermolecular hydrogen bonding interactions (Fig. 2.11a).

The 2D fingerprint plot of complex **VI** further emphasizes the significance of the O–H···O interactions in directing the arrangement of crystal structure in **VI** (Figure 2.11b). The gray region observed in Fig. 2.11b reflects the other intermolecular contacts apart from the reciprocal O···H contacts (O–H···O hydrogen bonding interactions) which are mainly displayed in blue (37.4%). These hydrogen bonding interactions are presented

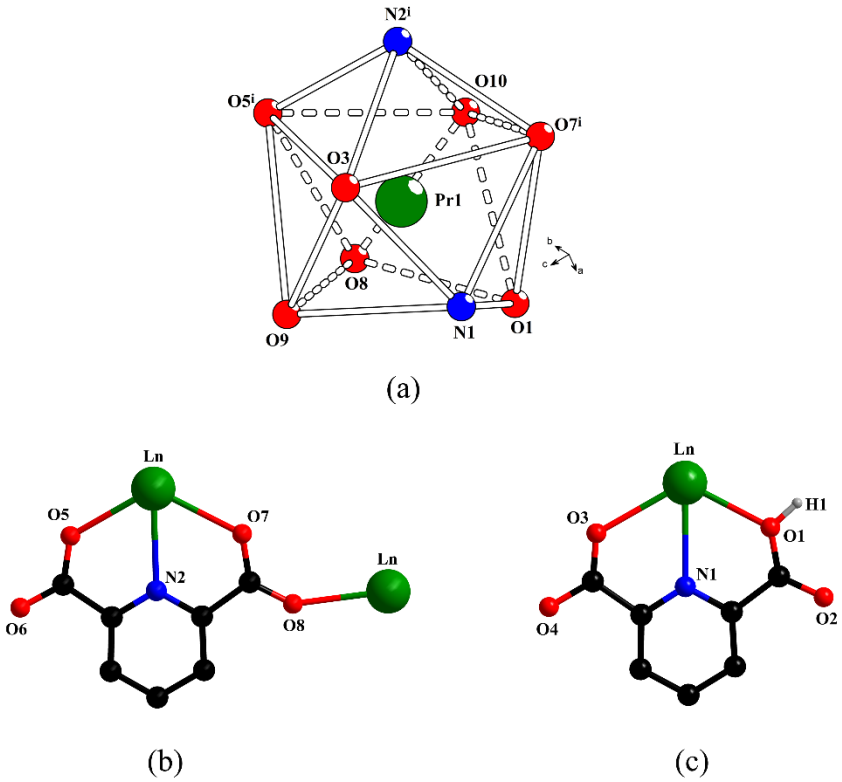

Fig. 2.8 Illustrations showing (a) the *SAPRS*-{PrO_7N_2} unit, and coordination modes of (a) pdc^{2-} ligand, and (c) $Hpdc^{-}$ ligand. Hydrogen atoms are omitted for clarity except for H1. Symmetry codes: (i) *x*, 0.5-*y*, -0.5+*z*.

as a characteristic pair of spikes at the bottom left of the plot (short d_i and d_e). The upper one refers to the donor atom and the lower one refers to the acceptor [19,22,31]. Fig. 2.11c shows the relative contributions to the Hirshfeld surface area from the O···H (*i.e.* O–H···O), N···H (*i.e.* O–H···N), C···H (*i.e.* C–H···π), C···C (*i.e.* π···π) and the others interaction such as the vdW close contacts for **VI**-**VIII**. If one disregards the other close contacts which are mainly H···H (vdW) interactions, the O···H (37.4% for **VI**, 34.1% for **VII**, and 35.5% for **VIII**) contacts have the highest share of the Hirshfeld surface in these three structures. The C···H or H···C contacts add up to 9.7%, 13.8%, and 12.2% of the surfaces for **VI**, **VII**, and **VIII**, respectively. These contacts come from the reciprocal close space between the hydrogen atoms on the pyridyl ring on the 1D chain and π electron of the pyridyl ring on the adjacent chain. There are no significant N···H (O–H···N interactions) and C···C (π-stacking interactions) contacts observed in these complexes.

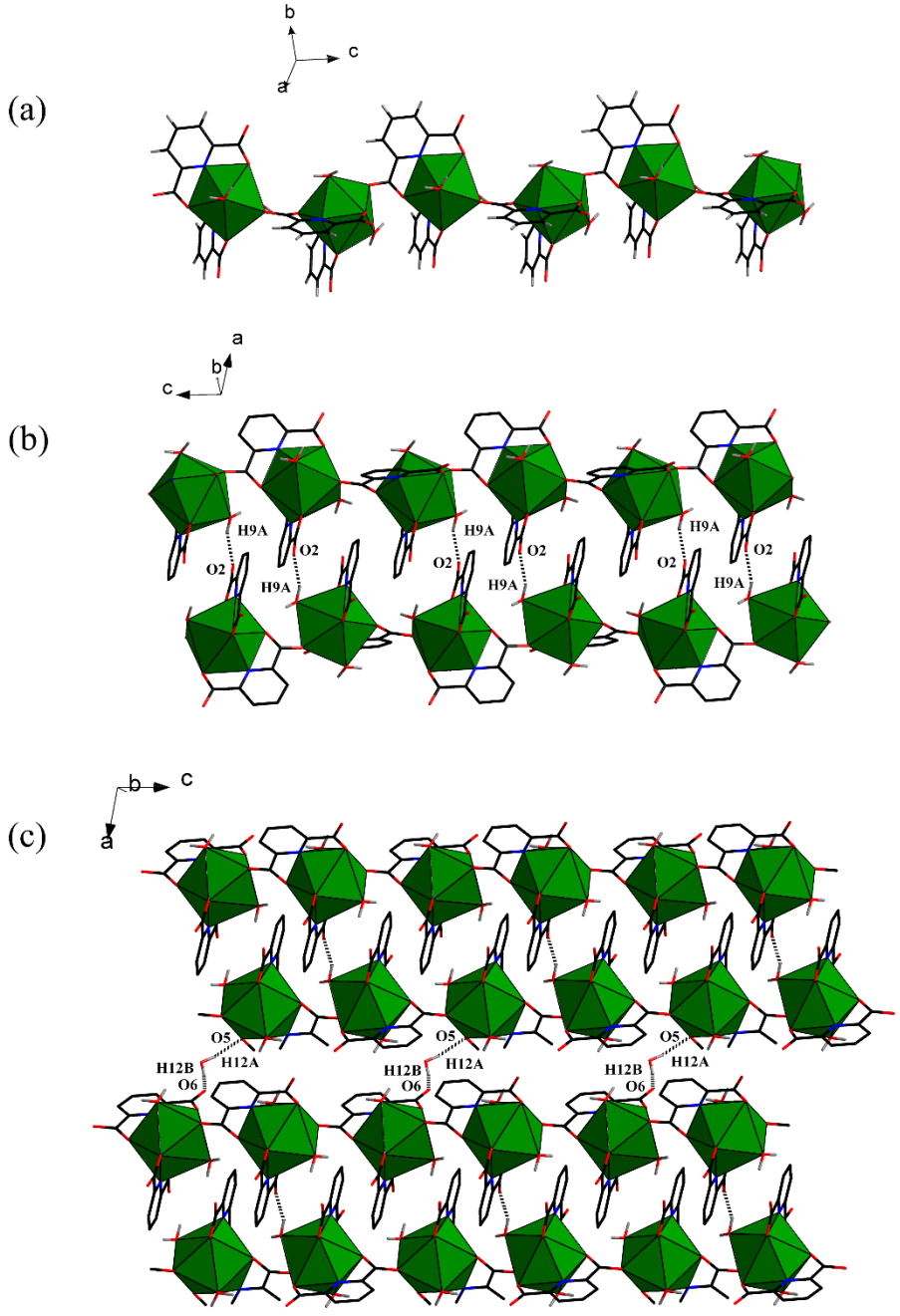

Fig. 2.9 Illustrations of (a) 1D coordination chain, (b) the infinite ladder-like structure, and (c) the 2D supramolecular sheet of **VI** (as a representative of **VII** and **VIII**).

These relative contributions clearly show that the packing system adopted by **VI-VIII** is primarily accounted for by the intermolecular O–H···O interactions.

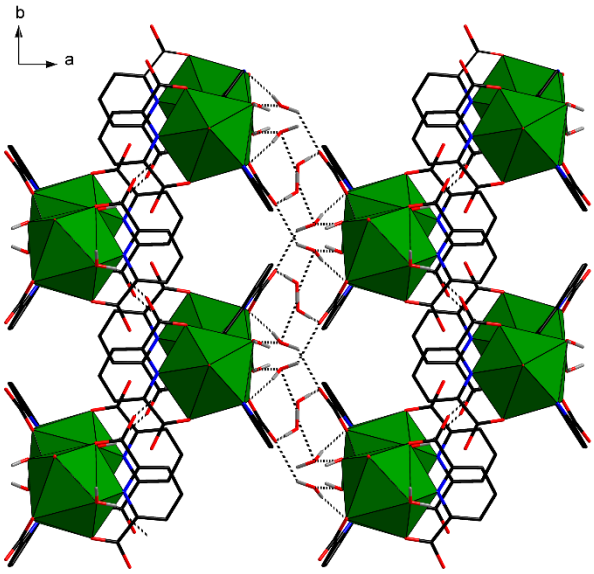

Fig. 2.10 View of the 3D supramolecular network of **VI** constructed from the hydrogen bonding interactions.

2.3.4 Thermogravimetric behaviors of V and VI

As clearly shown in Fig. 2.12, both complexes **V** and **VI** exhibited similar thermogravimetric behaviors. The first weight losses in the range of 35-200 ^{o}C attribute to the removal of coordinated water molecules; calc. = 16.76%, exp. = 17.4% for **V** and calc. = 16.02%, exp. = 17.2% for **VI**. After the loss of the water molecules, the two structures showed rather different weight loss patterns. Complex **V** showed a gradual weight loss over a wide range of temperature, *i.e.* 200-470 ^{o}C, after which its weight was abruptly decreased until 550 ^{o}C. This abrupt weight loss should be due to the decomposition of the organic ligands. After the heating at 1000 ^{o}C, the decomposition of the framework leading to Gd_2O_3 (calc. 42%, exp. 36%) can be assumed. In the case of **VI**, the weight loss pattern is poorly defined and cannot be interpreted with only the TGA results. The decomposition of the organic molecules and therefore the framework can be assumed. After the heat treatment at 1000 ^{o}C, Pr_4O_7 (calc. 30%, exp. 31%) was presumably yielded. According to the PXRD patterns, both structures apparently lost the long-range crystallinity after the liberation of the water molecules. The higher decomposition temperature of **V** is nonetheless consistent with the higher stability of its 3D coordination framework comparing with that of 1D coordination network of **VI**.

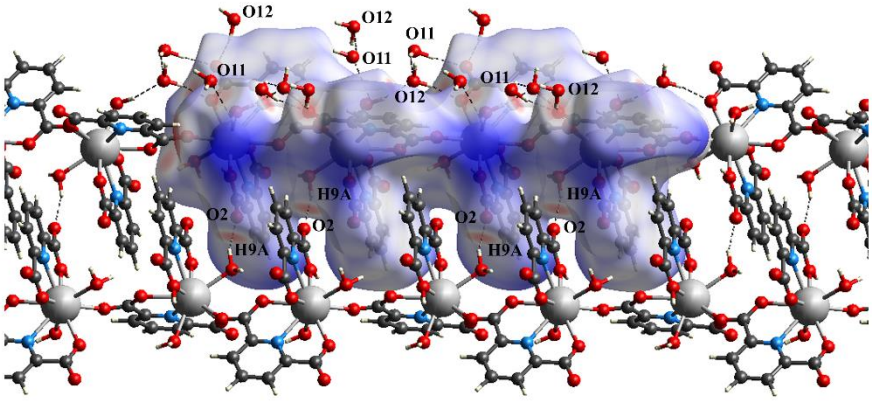

(a)

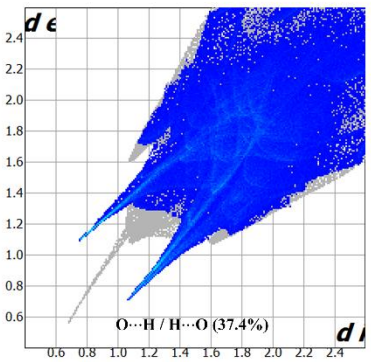

(b)

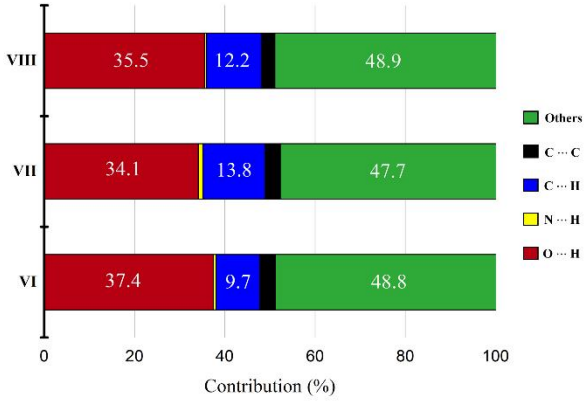

(c)

Fig. 2.11 Views of (a) the 3D Hirshfeld surface of **VI** mapped with d_{norm}, (b) the O···H contribution to the 2D fingerprint plot of **VI**, and (c) relative contributions to the Hirshfeld surface from various intermolecular contacts in **VI**-**VIII**.

2.3.5 UV-Vis and photoluminescence studies

Since the products synthesized by the microwave heating provide some unknown phases in PXRD pattern, the UV-Vis and photoluminescence spectra were collected only for the products yielded from the conventional heating of which every phase could be identified. The UV-Vis absorption spectra of all the samples synthesized by conventional heating under reflux compared with that of the H_2pdc ligand are exhibited in Fig. 2.13. The H_2pdc ligand shows characteristic absorption of the aromatic ring situated at *ca*. 219 and 272 nm both of which correspond to π-π* electronic transitions [32]. Whilst the complexes exhibit similar UV-Vis absorption bands to that of the free ligand which can

be attributed to ligand-centered π-π* transition, the absorption around 260-285 nm splits into three peaks. This can be resulted from the increased molecular rigidity in molecular structure of the ligand upon the coordination to the Ln^{III} ions. Along the lanthanide series from Pr to Gd complexes, the features in the 260-285 nm region slightly blue shift which is consistent with the stronger coordination bonding between the ligand and the Ln^{III} ion with smaller sizes.

The photoluminescence spectra of the synthesized samples compared with that of the H_2pdc ligand are shown in Fig. 2.14. Upon the excitation at 255 nm, the free H_2pdc ligand exhibits a broad band with several peaks covering almost an entire visible region which can be assigned to the pyridyl ring π*-π emission [33]. The effect of the various degrees of deprotonation on the energy of the triplet state of the ligand was negligible according to the previous report [33]. Being suitably sensitized by the ligand, the Eu complexes (**IV**+**X**) exhibit the intense characteristic red emissions which can be ascribed to the electronic transitions from the first excited $^5D_0$ state to the ground multiplets ^7F_J (J=0-4). In the case of Pr (**VI**), Nd (**II**+**VII**) and Sm (**III**+**VIII**+**IX**) complexes, they show only weak emissions that are resulted from the redundant differences between the triplet state of the ligand and the first excited states of the Ln^{III} ions resulting in poor energy transfer [33]. Moreover, the large numbers of the excited states in Pr (**VI**) and Nd (**II**+**VII**) may additionally perform energy loss through the non-radiative pathways [34]. Compared with the spectrum of free H_2pdc ligand, the greater molecular rigidity upon coordination to the metal centers leads to an occurrence of the emission band centered at 300 nm which can be assigned to the ligand centered π*-π emission [6]. The photoluminescence spectrum of Gd complex (**V**) was not collected because the extremely high energies of the excited states of Gd^{III} ion prevent the energy transfer process from any known ligands and the *f-f* transitions are consequently not available [35].

2.4 Conclusions

In summary, ten Ln-CPs have been synthesized using the H_2pdc ligand and two different heating techniques, namely the conventional heating under reflux and the microwave heating. The microwave heating yields the kinetically favorable cubic $Pa\bar{3}$ structures **I**-**V**, while the conventional heating provides three groups of isostructural crystals: (i) the monoclinic $P2_1/c$ structures **VI**-**VIII**, (ii) the cubic $Ia\bar{3}$ structures **IX** and

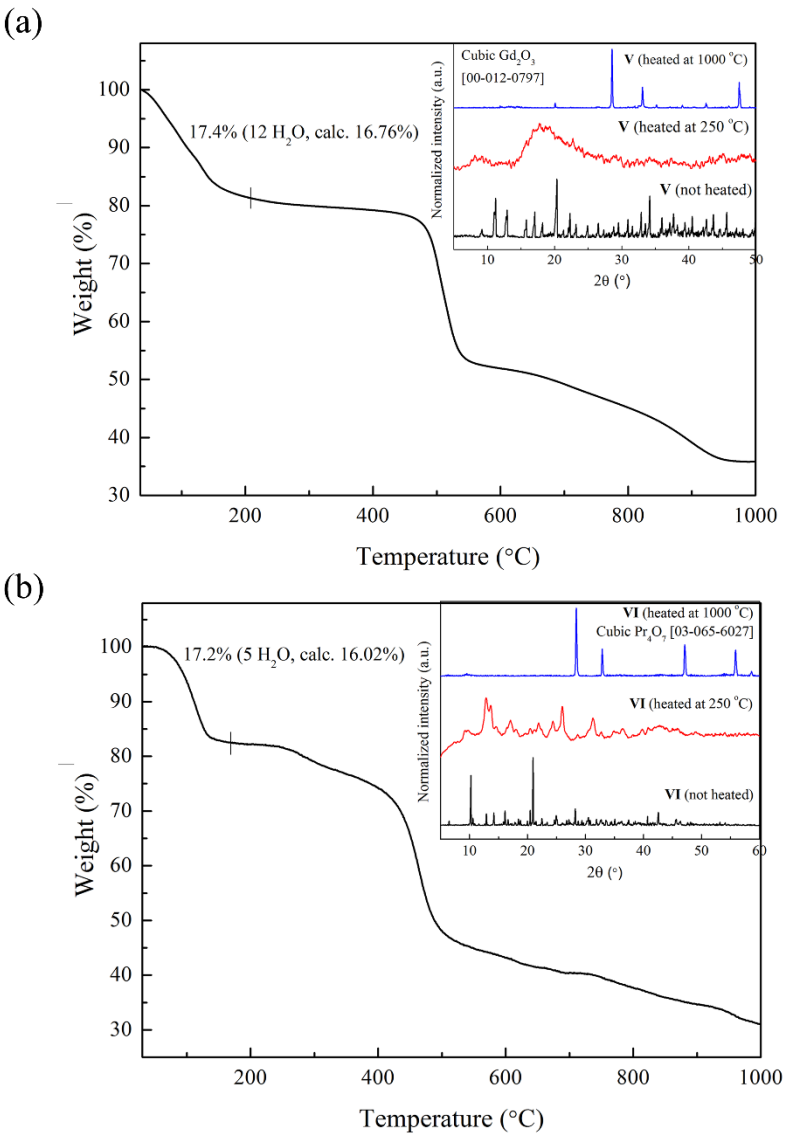

Fig. 2.12 Thermogravimetric curves of (a) **V** and (b) **VI** with the corresponding PXRD patterns in the insets.

X, and (iii) the cubic $Pa\bar{3}$ structures **II**, **III**, **IV**, and **V**. The isostructural $Pa\bar{3}$ complexes **I-V** exhibit the infinite linkage of *SAPRS*-{LnO_8N} units leading to the construction of 3D tubular structures with four discrete 1D channels extending in four <1 1 1> directions. Inside the channels, there are chloride anions transfixing with coordinated water molecules through hydrogen bonding interactions. The $Ia\bar{3}$ complexes **IX** and **X** which are supramolecular isomers of **III** and **IV**, respectively, are comprised of the Δ stereoisomeric *SAPRS*-{LnO_8N} units. Whilst those included in **III** and **IV** are Λ enantiomeric counterpart. Both cubic structures $Pa\bar{3}$ and $Ia\bar{3}$ can be simplified to two

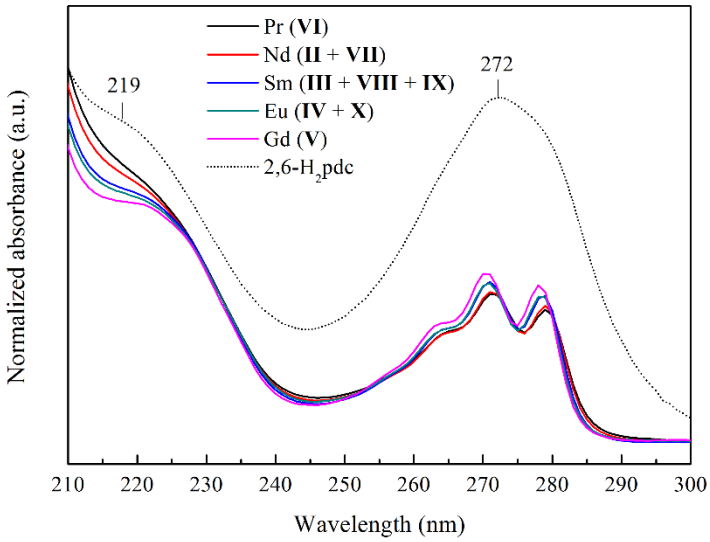

Fig. 2.13 UV-Vis spectra of the synthesized complexes compared with that of H_2pdc.

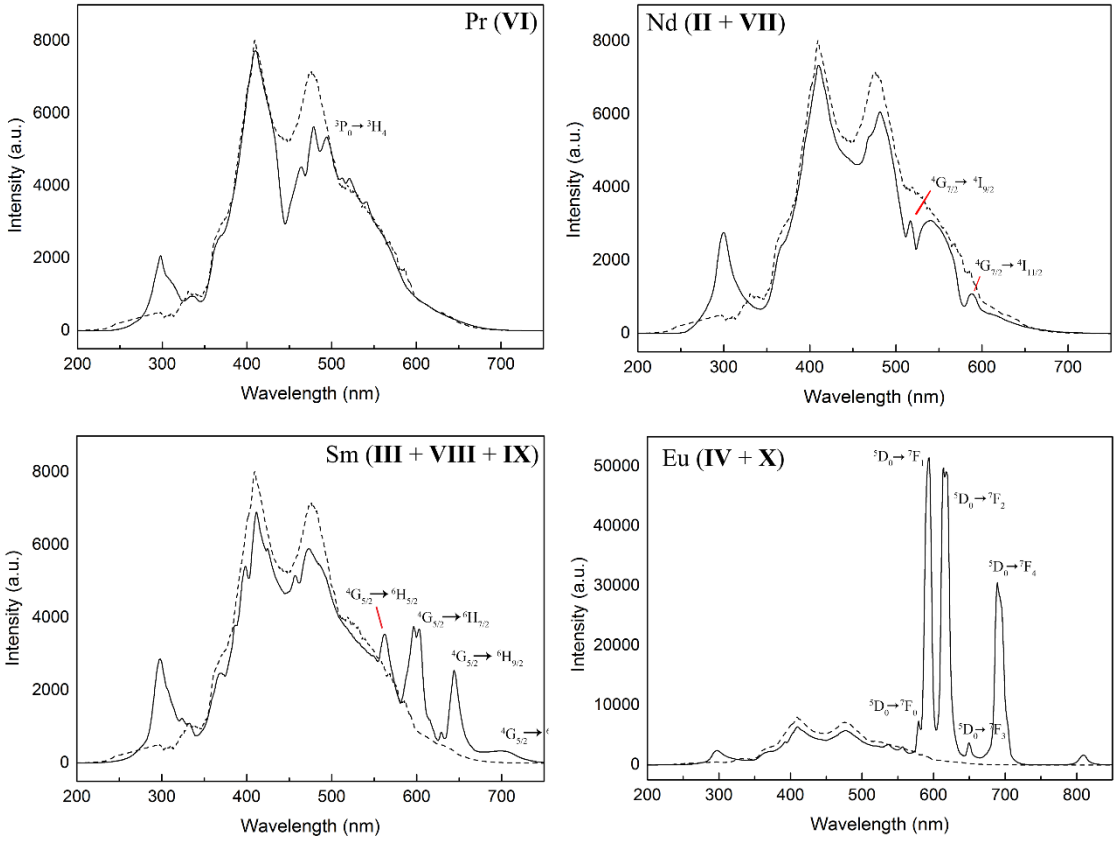

Fig. 2.14 Photoluminescence spectra of the synthesized complexes (solid line) compared with that of free H2pdc ligand (dash line).

interpenetrating unimodal **lcs** and **pcu** nets. In the case of the monoclinic $P2_1/c$ structures **VI-VIII**, since the existence of partly deprotonated ligand ($Hpdc^-$) which obstructs the formation of multi-dimensional coordination framework, they exhibit 3D supramolecular networks constructed by the hydrogen bonding interactions of the infinite 1D coordination chains. The formation of these 3D supramolecular networks in **VI-VIII** by the hydrogen bonding interactions can be vividly presented by the Hirshfeld surface analysis. According to the TGA results, the cubic complexes showed higher thermal stability than the monoclinic complexes. The UV-Vis spectroscopic studies of the complexes reveal the significant alteration of the absorption bands compared with free H_2pdc ligand. Additionally, the photoluminescence studies exhibit moderate ability of the ligand in sensitizing the characteristic emissions of the Ln^{III} ions.

REFERENCES

[1] Yang, L., Xu, J., Xia, J., Liu, Y., Wang, L., and Fan, Y., "Two novel indium coordination polymers derived from 2,6-pyridinedicarboxylate ligand: Syntheses, structures and photoluminescent properties," Journal of Molecular Structure, Vol. 1075, No., 2014, pp. 279-285.

[2] Song, S., Shao, C., Zhang, H., Zhang, W., Yang, L., Ren, T., and Bu, Z., "A 2D Hydrogen-Bonded 1D Coordination Network of Pr(III) with Pyridine-2,6-Dicarboxylic Acid: Hydrothermal Synthesis, Structure, and Luminescent Properties," Synthesis and Reactivity in Inorganic, Metal-Organic, and Nano-Metal Chemistry, Vol. 43, No. 2, 2013, pp. 169-174.

[3] Groom, C.R., Bruno, I.J., Lightfoot, M.P., and Ward, S.C., "The Cambridge Structural Database," Acta Crystallographica Section B: Structural Science, Vol. 72, No. 2, 2016, pp. 171-179.

[4] Hao, L.-J. and Yu, T.-L., "catena-Poly[[[diaqua(6-carboxypyridine-2-carboxylato-κ3O,N,O′)gadolinium(III)]-μ-pyridine-2,6-dicarboxylato-κ4N,O,O′:O″] tetrahydrate]," Acta Crystallographica Section E: Structure Reports Online, Vol. 63, No. 7, 2007, pp. m1967-m1967.

[5] Ramezanipour, F., Aghabozorg, H., Shokrollahi, A., Shamsipur, M., Stoeckli-Evans, H., Soleimannejad, J., and Sheshmani, S., "Different complexation behavior of a proton transfer compound obtained from 1,10-phenanthroline and pyridine-2,6-dicarboxylic acid with InIII and CeIII: Synthesis, crystal structures and solution studies," Journal of Molecular Structure, Vol. 779, No. 1-3, 2005, pp. 77-86.

[6] Wang, P., Fan, R.-Q., Liu, X.-R., Yang, Y.-L., and Zhou, G.-P., "Fluorescence Properties Change of Lanthanide Coordination Polymers Dispersed in Mesoporous SBA-15 by Energy Transition Process," Journal of

Inorganic and Organometallic Polymers and Materials, Vol. 22, No. 4, 2012, pp. 744-755.

[7] Prasad, T.K., Sailaja, S., and Rajasekharan, M.V., "1-Dimensional and 2-dimensional coordination network structures in the Ba-Ce-dipicH2 system (dipicH2 = dipicolinic acid)," Polyhedron, Vol. 24, No. 12, 2005, pp. 1487-1496.

[8] Pan, L., Frydel, T., Sander, M.B., Huang, X., and Li, J., "The Effect of pH on the Dimensionality of Coordination Polymers," Inorganic Chemistry, Vol. 40, No. 6, 2001, pp. 1271-1283.

[9] Fan, S.-R. and Zhu, L.-G., "Influence of the Reaction Conditions on the Self-assembly of Lead(II) 5-Sulfosalicylate Coordination Polymers with Chelating Amine Ligands," Inorganic Chemistry, Vol. 45, No. 19, 2006, pp. 7935-7942.

[10] Song, Y., Feng, M.-L., Wu, Z.-F., and Huang, X.-Y., "Solvent-assisted construction of diverse Mg-TDC coordination polymers," CrystEngComm, Vol. 17, No. 6, 2015, pp. 1348-1357.

[11] Robin, A.Y. and Fromm, K.M., "Coordination polymer networks with O- and N-donors: What they are, why and how they are made," Coordination Chemistry Reviews, Vol. 250, No. 15-16, 2006, pp. 2127-2157.

[12] Stock, N. and Biswas, S., "Synthesis of Metal-Organic Frameworks (MOFs): Routes to Various MOF Topologies, Morphologies, and Composites," Chemical Reviews, Vol. 112, No. 2, 2012, pp. 933-969.

[13] Sheldrick, G., "A short history of SHELX," Acta Crystallographica Section A: Foundations of Crystallography, Vol. 64, No. 1, 2008, pp. 112-122.

[14] Dolomanov, O.V., Bourhis, L.J., Gildea, R.J., Howard, J.A.K., and Puschmann, H., "OLEX2: a complete structure solution, refinement and analysis program," Journal of Applied Crystallography, Vol. 42, No. 2, 2009, pp. 339-341.

[15] Sheldrick, G.M., Program name. 1996, University of Göttingen: Germany.

[16] Spek, A., "Single-crystal structure validation with the program PLATON," Journal of Applied Crystallography, Vol. 36, No. 1, 2003, pp. 7-13.

[17] Spackman, M.A. and Jayatilaka, D., "Hirshfeld surface analysis," CrystEngComm, Vol. 11, No. 1, 2009, pp. 19-32.

[18] McKinnon, J.J., Mitchell, A.S., and Spackman, M.A., "Hirshfeld Surfaces: A New Tool for Visualising and Exploring Molecular Crystals," Chem. Eur. J., Vol. 4, No. 11, 1998, pp. 2136-2141.

[19] McKinnon, J.J., Spackman, M.A., and Mitchell, A.S., "Novel tools for visualizing and exploring intermolecular interactions in molecular crystals," Acta Crystallographica Section B: Structural Science, Vol. 60, No. 6, 2004, pp. 627-668.

[20] Hosseini, S.A., Mahmoudi, G., Garczarek, P., Hazendonk, P., Abedi, M., and Servati Gargari, M., "Crystal structures and Hirshfeld surface analysis calculations of mercury(II) complexes with a diiminopyridine ligand," Journal of Molecular Structure, Vol. 1105, No., 2016, pp. 159-168.

[21] Zaręba, J.K., Białek, M.J., Janczak, J., Zoń, J., and Dobosz, A., "Extending the Family of Tetrahedral Tectons: Phenyl Embraces in Supramolecular Polymers of Tetraphenylmethane-based Tetraphosphonic Acid Templated by Organic Bases," Crystal Growth and Design, Vol. 14, No. 11, 2014, pp. 6143-6153.

[22] McKinnon, J.J., Jayatilaka, D., and Spackman, M.A., "Towards quantitative analysis of intermolecular interactions with Hirshfeld surfaces," Chemical Communications, Vol. No. 37, 2007, pp. 3814-3816.

[23] Wolff, S.K., Grimwood, D.J., McKinnon, J.J., Turner, M.J., Jayatilaka, D., and Spackman, M.A., Crystal Explorer Ver. 3.1. 2013: University of Western Australia, Perth, Australia.

[24] Ghosh, S.K. and Bharadwaj, P.K., "Coordination Polymers of La(III) as Bunched Infinite Nanotubes and Their Conversion into an Open-Framework Structure," Inorganic Chemistry, Vol. 44, No. 9, 2005, pp. 3156-3161.

[25] Ghosh, S.K. and Bharadwaj, P.K., "Coexistence of Water Dimer and Hexamer Clusters in 3D Metal-Organic Framework Structures of Ce(III) and Pr(III) with Pyridine-2,6-dicarboxylic Acid," Inorganic Chemistry, Vol. 42, No. 25, 2003, pp. 8250-8254.

[26] Liu, S.-H., Meng, Q.-J., and Li, Y.-Z., "catena-Poly[[[diaqua(6-carboxypyridine-2-carboxylato-κ3N,O,O′)samarium(III)]-μ-pyridine-2,6-dicarboxylato-κ4N,O,O′:O″] tetrahydrate]," Acta Crystallographica Section E: Structure Reports Online, Vol. 61, No. 6, 2005, pp. m1111-m1113.

[27] Jhung, S.H., Jin, T., Hwang, Y.K., and Chang, J.-S., "Microwave Effect in the Fast Synthesis of Microporous Materials: Which Stage Between Nucleation and Crystal Growth is Accelerated by Microwave Irradiation?," Chem. Eur. J., Vol. 13, No. 16, 2007, pp. 4410-4417.

[28] Douglas, B.E., "The Lanthanide contraction," Journal of Chemical Education, Vol. 31, No. 11, 1954, pp. 598.

[29] Blatov, V.A., Shevchenko, A.P., and Proserpio, D.M., "Applied Topological Analysis of Crystal Structures with the Program Package ToposPro," Crystal Growth and Design, Vol. 14, No. 7, 2014, pp. 3576-3586.

[30] Zou, J.-P., Wen, Z.-H., Peng, Q., Zeng, G.-S., Xing, Q.-J., and Chen, M.-H., "A 1-D chain praseodymium complex with chelidamic acid: synthesis, structure, and optical properties," Journal of Coordination Chemistry, Vol. 62, No. 20, 2009, pp. 3324-3331.

[31] Potts, S.V. and Barbour, L.J., "Solvent-mediated conformational similarities within a series of 1D coordination polymers constructed from a new flexible ditopic bis-imidazole ligand," New Journal of Chemistry, Vol. 34, No. 11, 2010, pp. 2451-2457.

[32] Tao, C., Du, K., Yin, Q., Zhu, J., Yan, H., Zhu, F., and Zhang, L., "Pyridine-2,6-dicarboxylic acid for the sensitization of europium(iii) luminescence with very long lifetimes," RSC Advances, Vol. 5, No. 72, 2015, pp. 58936-58942.

[33] Massaro, R.D. and Blaisten-Barojas, E., "Density functional theory study of dipicolinic acid isomers and crystalline polytypes," Computational and Theoretical Chemistry, Vol. 977, No. 1-3, 2011, pp. 148-156.

[34] Cui, Y., Chen, B., and Qian, G., "Lanthanide metal-organic frameworks for luminescent sensing and light-emitting applications," Coordination Chemistry Reviews, Vol. 273-274, No., 2014, pp. 76-86.

[35] Vogler, A. and Kunkely, H., "Excited state properties of lanthanide complexes: Beyond ff states," Inorganica Chimica Acta, Vol. 359, No. 12, 2006, pp. 4130-4138.